RSC Advances

PAPER

View Article Online
View Journal | View Issue

Check for updates

Cite this: *RSC Adv.*, 2023, **13**, 19888

Colloidal self-assembly of soft neural interfaces from injectable photovoltaic microdevices†

Haiyan Jia,* Zhangjun Huang, Murat Kaynak and Mahmut Selman Sakar*

Biomimetic retinas with a wide field of view and high resolution are in demand for neuroprosthetics and robot vision. Conventional neural prostheses are manufactured outside the application area and implanted as a complete device using invasive surgery. Here, a minimally invasive strategy based on *in situ* self-assembly of photovoltaic microdevices (PVMs) is presented. The photoelectricity transduced by PVMs upon visible light illumination reaches the intensity levels that could effectively activate the retinal ganglion cell layers. The geometry and multilayered architecture of the PVMs along with the tunability of their physical properties such as size and stiffness allow several routes for initiating a self-assembly process. The spatial distribution and packing density of the PVMs within the assembled device are modulated through concentration, liquid discharge speed, and coordinated self-assembly steps. Subsequent injection of a photocurable and transparent polymer facilitates tissue integration and reinforces the cohesion of the device. Taken together, the presented methodology introduces three unique features: minimally invasive implantation, personalized visual field and acuity, and a device geometry adaptable to retina topography.

Received 29th May 2023
Accepted 26th June 2023

DOI: 10.1039/d3ra03591c

rsc.li/rsc-advances

Open Access Article. Published on 03 July 2023. Downloaded on 12/24/2025 11:41:32 PM.
This article is licensed under a Creative Commons Attribution-NonCommercial 3.0 Unported Licence.

1. Introduction

The number of people with vision impairment is currently around 237 million and continues to grow with the increasing human lifespan,[1] therefore there exists a pressing need to address these impairments. Retinal prostheses[2–7] consisting of microfabricated electrode arrays have emerged as an effective strategy to cure blindness caused by retinitis pigmentosa[8] and macular degeneration.[9] Notably, the coarse recognition of simple objects has been achieved in clinical trials with electrode arrays powered by inductive coils.[10,11] Achieving high resolution and sensitivity with low aberration in imaging is the holy grail in the field. Among different material formulations, organic photovoltaic thin films hold great potential because they offer facile processing, biocompatibility, and mechanical conformity. A foldable organic photovoltaic device that consists of 2000 pixels and 46.3 degrees of visual angle has been recently developed as an epi-retinal prosthesis.[6,12,13] To reduce the pixel size further, a biomimetic hemispherical perovskite nanowire array has been developed.[14]

There are a number of outstanding challenges. Considering the importance of visual acuity and field of view, the density and coverage of photovoltaic elements must be maximized. Increasing the density of those elements naturally decreases the flexibility of the prosthetic device. On the other hand, the prosthesis must perfectly conform to the non-planar geometry of the retinal surface, which varies from patient to patient.[6] Aside from this fundamental tradeoff, surgery is unavoidable during the implantation of a retina-sized device, making the procedure invasive. In all the aforementioned examples, the devices were fabricated using standard cleanroom processes, assembled outside the eye, and implanted through surgical operations.

Assembling retinal prostheses from a suspension of colloidal devices, following a ship-in-a-bottle construction strategy, may address all these challenges. This strategy may also reduce the costs through mass production and provide a more personalized therapeutic solution. Recent work has demonstrated that subretinal injection of photovoltaic nanoparticles could mediate light-invoked stimulation of neurons and rescue visual functions.[15–17] Therefore, it is conceivable that a device assembled from photovoltaic microparticles may serve as a functional prosthesis. Using photovoltaic microparticles, instead of nanoparticles, we could combine the superior performance, controllable deployment and hierarchical architecture of microfabricated devices with the reach, conformity and minimally invasiveness of nanotechnology. A number of interfacial self-assembly techniques have been introduced such as Langmuir–Blodgett deposition,[18] spin-coating,[19] air–liquid,[20] and water/oil interfacial assembly[21,22] to fabricate functional thin films with close-packed arrangements. Alternatively, assembly techniques based on convective and capillary flows have been developed to form colloidal assemblies with preprogrammed

Institute of Mechanical Engineering, Ecole Polytechnique Fédérale de Lausanne, Lausanne CH-1015, Switzerland. E-mail: zjjiahaiyan@163.com; selman.sakar@epfl.ch

† Electronic supplementary information (ESI) available. See DOI: https://doi.org/10.1039/d3ra03591c

© 2023 The Author(s). Published by the Royal Society of Chemistry

Open Access Article. Published on 03 July 2023. Downloaded on 12/24/2025 11:41:32 PM.
This article is licensed under a Creative Commons Attribution-NonCommercial 3.0 Unported Licence.

patterns that are practical in printing,[23] point-of-care medical diagnostics,[24,25] electronics[26] and robotics.[27]

The next milestone is the fabrication of biocompatible photovoltaic microdevices and the development of *in situ* self-assembly techniques within the eye as a route for retinal neuroprosthetics—the focus of our study. Here, we combined state-of-the-art techniques in microfluidics, inorganic and organic chemistry, and colloidal science to synthesize photovoltaic microdevices with high-throughput and reproducibility. The colloidal device consists of a biocompatible transparent polymer core covered by a thin layer of conducting polymer serving as anode, a photoactive organic shell that creates excitons when exposed to light, and a titanium film serving as cathode. We extensively characterized the photoelectric response of the devices to physiologically relevant illumination to optimize their design. We investigated directed colloidal self-assembly methods with which the devices could be assembled into various monolayer patterns on confined and complex surfaces. The geometry and multilayered architecture of the devices along with the tunability of their physical properties such as size and stiffness allow several routes for the development of a new class of soft neural interfaces that can be self-assembled directly on the target tissue in a minimally invasive fashion.

2. Results and discussion

The overall concept is illustrated in Fig. 1a. We introduce functional spherical photovoltaic microdevices (PVMs), which serve as both transducers and building blocks for constructing a prosthetic device directly on curved substrates such as the retina.

2.1 Design and fabrication of PVMs

To streamline the process of self-assembly, we designed the organic photovoltaic pixels as multilayered core–shell microspheres, denoted as PVMs (Fig. 1b). A PVM consists of a biocompatible, photo-curable, and transparent core made of poly(trimethylolpropane ethoxylate triacrylate) (PTPETA). The core sphere is surrounded by an inner anode made of poly(3,4-ethylenedioxythiophene):poly(styrenesulfonate) (PEDOT:PSS), a middle photovoltaic semiconductor layer made of poly(3-hexylthiophene-2,5-diyl):[6,6]-phenyl-C_{61}-butyric acid methyl ester (P3HT:PCBM), and an outermost metallic electrode made of titanium (Ti). This version of PVMs is referred to as PTPETA@PEDOT:PSS@P3HT:PCBM@Ti.

We assumed that the transduction mechanism of PVMs is the same as the flat 2D photovoltaic devices, which have been well-studied in the literature for the development of retinal prosthesis.[28–31] Upon illumination, the photovoltaic P3HT:PCBM layer produces electrons and holes. The PEDOT:PSS anode works as a virtual ground to accumulate holes during the illumination cycle, meanwhile, the electrons accumulate at the cathode and polarize the electrolyte. Once the light is off, holes recombine with electrons to quench charges. Ti is a widely used implantable material with good mechanical and electrochemical stability. The thin titanium oxide layer on the surface of Ti acts as a capacitive charge-injection material,[6,31] exposing the electrolyte and injecting photocurrent without transferring electrons into the solution. Therefore, the whole process might be considered as the charging and discharging of a thin-film capacitor.

We present a facile route to mass produce PVMs in Fig. 2a. The core–shell PTPETA@PEDOT:PSS microspheres were fabricated with a one-step formation of TPETA@PEDOT:PSS core–shell double emulsion using a flow-focusing microfluidic device with two junctions.[32,33] This process was followed by the photopolymerization of the TPETA core, and thermally crosslinking and drying of the PEDOT:PSS shell, consecutively. The phase was designed to be in oil/water/oil configuration: TPETA with

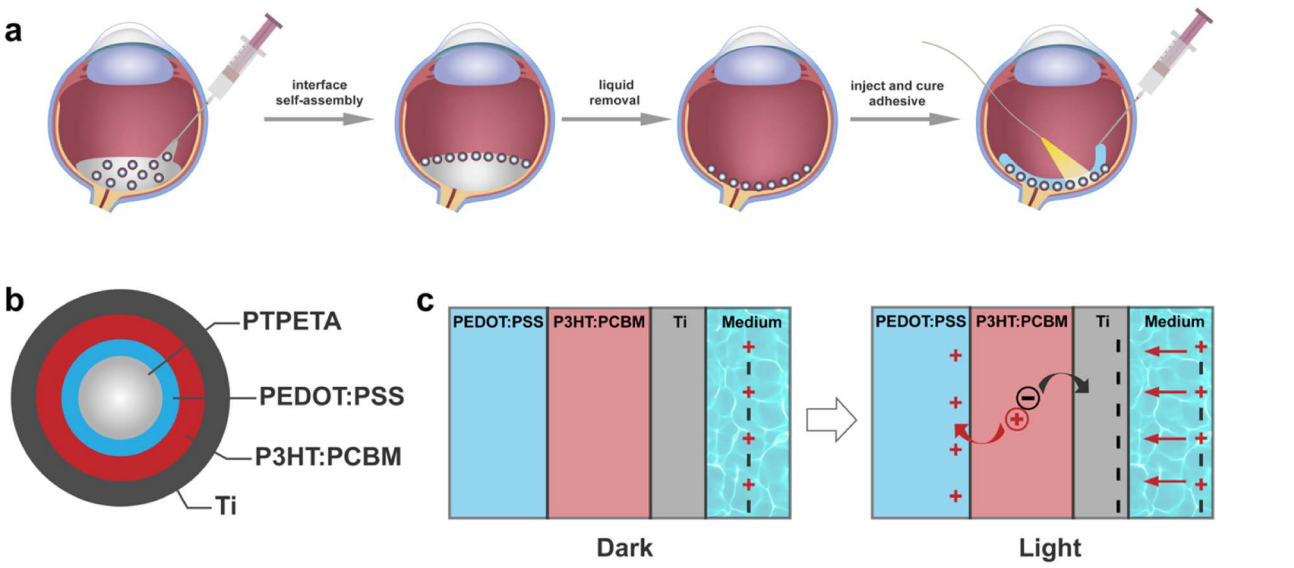

Fig. 1 Design, working principle, and guided self-assembly of injectable PVMs. (a) Schematic illustration of the proposed methodology for the *in situ* construction of a retinal prosthesis. (b) PVMs consist of multilayers of functional electronic materials. (c) Photoelectric transduction mechanism based on photovoltaic properties of PVMs.

Open Access Article. Published on 03 July 2023. Downloaded on 12/24/2025 11:41:32 PM.
This article is licensed under a Creative Commons Attribution-NonCommercial 3.0 Unported Licence.

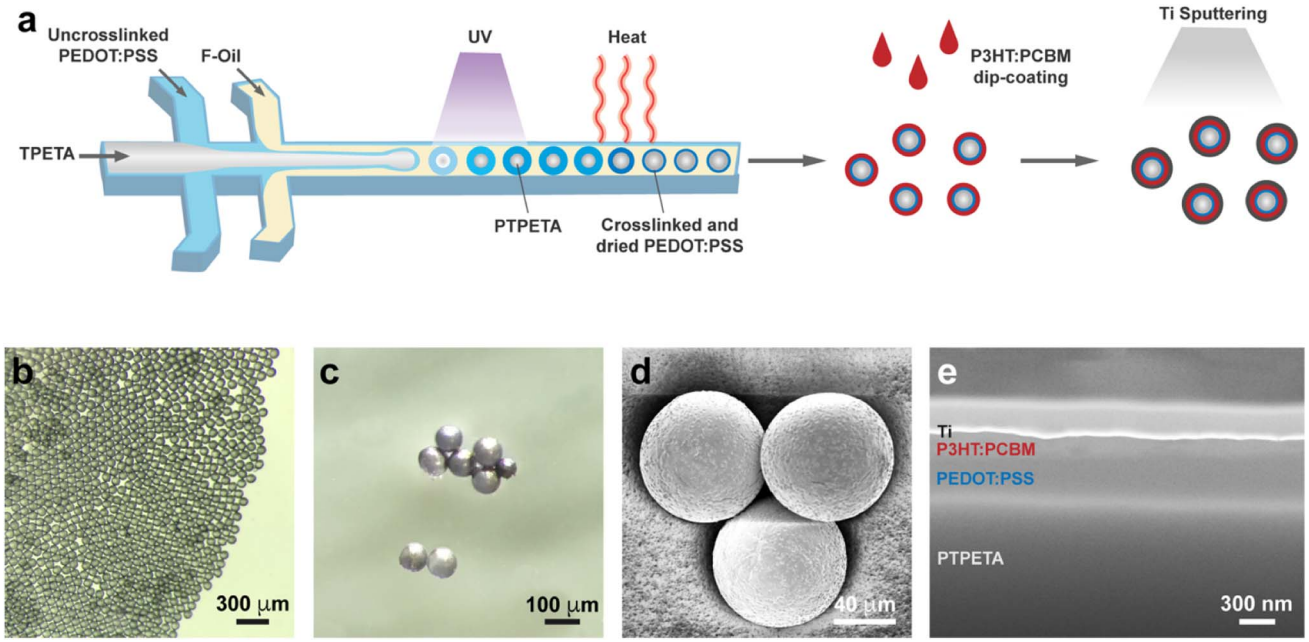

Fig. 2 Microfabrication of PVMs. (a) The polymer core of the PVM is fabricated using microfluidic photolithography. The polymer core is coated with a thin film of PEDOT:PSS through a thermal coating process. Additional layers of photovoltaic material and metal are deposited using dip-coating and sputtering, respectively. (b) Optical image of a collection of core–shell PTPETA@PEDOT:PSS microspheres. The fabrication process is high-throughput as thousands of PVMs can be fabricated within minutes. (c) Close-up optical image of PVMs showing a monodisperse size distribution. (d) Scanning electron microscopy image of three PVMs. The PVMs appear to have a smooth surface, indicating a conformal coating of PEDOT:PSS, P3HT:PCBM, and Ti around the spherical PTPETA substrate. (e) Scanning electron microscopy image showing the cross-sectional view of a PVM obtained by focused ion beam cutting. Different layers can be identified from visual contrast. They appear to be stacked on top of each other without showing signs of delamination.

photoinitiator as the inner phase, PEDOT:PSS aqueous solution with surfactant Tween 20 and crosslinker (3-glycidyloxypropyl) trimethoxysilane (GOPS) as the middle phase, and Novec 7500 with surfactant Pico-Surf as the continuous phase.

To generate the desired TPETA@PEDOT:PSS double emulsions, PEDOT:PSS drops must spontaneously engulf TPETA drops. We tuned interfacial tensions between the three phases using the following equations.[34]

$$S_A = \gamma_{BC} - (\alpha\gamma_{AC} + \gamma_{AB}) \quad (1)$$

$$\alpha = \left[1 + \left(\frac{R_A}{R_B}\right)^3\right]^{\frac{2}{3}} - \left(\frac{R_A}{R_B}\right)^2, \quad \alpha \in (0,1) \quad (2)$$

where S_A is the spreading coefficient; A, B, and C denote PEDOT:PSS, TPETA, and Novec 7500 phases, respectively. The interfacial tensions among the three phases are given by γ_{AB}, γ_{AC}, and γ_{BC}, respectively. R_A and R_B denote the radii of PEDOT:PSS and TPETA drop before engulfment, respectively. When $S_A > 0$, A engulfs B spontaneously.[34] In our formulation, the surfactant concentrations are as follows: 0.1% (w/w) Tween 20 in the PEDOT:PSS and 0.1% (w/w) Pico-Surf™ in the Novec 7500, respectively to obtain $\gamma_{AB} = 0.3$ mN m^{-1}, $\gamma_{AC} = 0.24$ mN m^{-1}, and $\gamma_{BC} = 4.45$ mN m^{-1}. For these values of interfacial tensions, S_A is positive, thus, TPETA is expected to be engulfed by PEDOT:PSS within the microfluidic channels.

Another important consideration is to tune the parameters so that every PEDOT:PSS drop is engulfed within a TPETA drop. To this end, we tuned the flow rates of the three phases until the inner TPETA phase starts to form a microfluidic jet (Fig. S1a†). By further tuning the flow rate of each phase, different size ratios of PTPETA core with respect to PEDOT:PSS coating were obtained (Fig. S1b†). In this work, we designed PVMs to have a diameter of 85 μm. The chosen flow rates are 0.8, 1, and 10 μl min^{-1} for TPETA, PEDOT:PSS, and Novec 7500, respectively. A monodisperse suspension of droplets was synthesized *en masse* (Fig. S1c†).

The first stage of microfabrication was completed with the photopolymerization of the TPETA core. To do so, the tubing where we collected the multi-layered droplets was irradiated under UV light (365 nm, 5 mW cm^{-2}) for four seconds. Next, the resulting PTPETA@PEDOT:PSS double emulsion was collected in Novec 7500 with 1% (w/w) Pico-Surf, and incubated at 93 °C. The water in the PEDOT:PSS phase evaporates due to the relatively high temperature, forcing PEDOT:PSS to form a thin layer covering the PTPETA core. Meanwhile, three covalent interactions involving (3-glycidyloxypropyl)trimethoxysilane (GOPS), PSS, and PTPETA sustained a homogeneous coverage and stability of PTPETA@PEDOT:PSS. These chemical interactions have been well-studied in the literature.[35,36] Briefly, reactions between epoxy rings of GOPS organosilane and –SO_3H groups of PSS, and reactions between methoxysilane groups of GOPS and ethoxy groups at the PTPETA surface improve the adhesion between PEDOT:PSS layer and PTPETA core. Notably, tripolymer of GOPS resulting from oligomerization *via* methoxysilane

© 2023 The Author(s). Published by the Royal Society of Chemistry

Open Access Article. Published on 03 July 2023. Downloaded on 12/24/2025 11:41:32 PM. This article is licensed under a Creative Commons Attribution-NonCommercial 3.0 Unported Licence.

groups also serves as a crosslinker for the PSS. In presence of an insufficient amount of GOPS in the PEDOT:PSS phase, PEDOT:PSS aggregated into semi-spheres and formed Janus particles with a PTPETA core (Fig. S2†). In this scenario, the PEDOT:PSS phase delaminated instantaneously upon submerging in an aqueous environment because of interfacial phenomena and the water solubility of PSS. To get uniform and stable PTPETA@PEDOT:PSS and to maintain satisfactory photovoltaic performance, 0.1% (v/v) GOPS was introduced into the PEDOT:PSS phase, following the results of another work.[12]

The second shell, P3HT:PCBM, was formed on the PTPETA@PEDOT:PSS by dip-coating (Fig. S3a†). The Ti electrode was sputtered on the outermost layer to obtain the final PVM (Fig. S3b†). To get full coverage of P3HT:PCBM and the anode, the dip-coating and sputtering processes were repeated at least 3 times. The role of the thicknesses of PEDOT:PSS and P3HT:PCBM layers on the photovoltaic performance of prosthetic devices has been studied extensively. When the PEDOT:PSS layer is thinner than 50 nm, the photoelectricity performance increases with the thickness of PEDOT:PSS. On the other hand, when this layer is thicker than 50 nm, the effect of thickness on performance is insignificant.[37,38] The optimal thickness of P3HT:PCBM is reported to be around 100 nm.[39,40] We based our design methodology on these reported data. The average thickness of PEDOT:PSS and P3HT:PCBM are 324 nm and 130 nm, respectively (Fig. 2c–e).

2.2 Characterization of PVMs

Increasing the thickness of the Ti layer would make a better cathode but the transparency decreases with thickness. To balance transparency and conductivity, we studied the role of Ti thickness on photosensitivity using flat 2D photovoltaic sheets. These sheets were fabricated on glass slides coated with indium tin oxide (ITO) that serve as the anode (Fig. 3a). We deposited PEDOT:PSS as the injection layer, P3HT:PCBM as the semiconductor layer, and Ti as the cathode. The photovoltage (PV) and photocurrent (PC) were measured upon illumination (0.67 mW mm^{-2}), with 1 s pulse duration and 3 s resting duration to allow total discharge. The thickness of Ti varied between 0 and 40 nm. In this range, PV and PC increase dramatically at first but start to decrease after exceeding 10 nm (Fig. 3b). In the absence of Ti cathodes, PV and PC were hardly detected, while devices with 10 nm of Ti in thickness exhibit the highest voltage of 0.12 V ($n = 15$). This drastic increase can be attributed to the high charge injection ability of Ti.[6,41] This data suggests that 10 nm thick Ti presented the optimal balance between transparency and conductivity. Accordingly, we fabricated PVMs with a 10 nm thick Ti layer for the remainder of the study.

Sensitivity to the light intensity is essential for a device to be used as a retinal prosthesis. In the remaining of the characterization, we made direct photoelectric measurements on PVMs that were residing on a gold (Au) coated glass substrate (Fig. 3c). We measured the PV and PC of PVMs upon illumination at increasing light intensities, starting from 0.005 to 1 mW mm^{-2} for 1 s pulse duration. Both PV (Fig. 3d) and PC (Fig. 3e) increased with light intensity for the chosen interval. The PVMs exhibited a mean peak value of 181.5 μA cm^{-2} at 0.035 mW mm^{-2}, a current density that is high enough to activate the retinal ganglion cells.[6,42–44] Both PC and PV reached the peak level within 100 ms of illumination and remained at this value over seconds, a response that is consistent with the capacitive nature of the device. At lower power densities, PVMs discharged as soon as the light source was turned off. At power densities higher than 0.175 mW mm^{-2}, a small amount of charge remained on the device that was discharged over time. 0.175 mW mm^{-2} is close to the recommended upper light level in workspaces, which would accommodate performing special visual tasks on objects with small features at exceptionally low contrast. Thus, the data suggest that PVMs injected into the retina may fully discharge in our daily life. Responsivity measures the input–output gain of a detector system. In the specific case of a photodetector, it measures the electrical output, photocurrent, per optical input power intensity. While PC monotonically increased with power intensity, responsivity showed the opposite trend (Fig. 3f).

Next, we evaluated the effect of pulse duration on the electrical performance of PVMs (Fig. 3g). Even at 10 ms pulse duration, we could detect the electrical signal where PV levels were comparable to the values reported for photo-activated retinal ganglion cells.[6,44] With the decreasing pulse duration, the peak values of PV decrease. For pulses shorter than 200 ms, a plateau on the PV signal is not detectable anymore (Fig. 3g), and the signal-to-noise ratio (SNR) gets progressively lower (Fig. S4†). PVMs could repeatedly fully discharge when stimulated with short pulses, even at 0.67 mW mm^{-2} illumination (Fig. S5†).

Sensitivity to periodic illumination is another critical performance metric. Fig. S6† shows PV recorded from PVMs illuminated at 10 Hz and 20 Hz with 10 ms light pulses of 0.175 mW mm^{-2}. PVMs are fully discharged between all pulses where the average PV of 10 pulses at 10 Hz and 20 Hz are identical. The data showed that PVMs could transduce flashing light with a frequency of 20 Hz, similar to human eyes. Moreover, PVMs could distinguish between illumination at 10 Hz and 20 Hz, and the photosensitivity did not show dependence on the illumination frequency. We repeatedly recorded PV of PVMs over 1500 pulses with 10 ms duration and 10 Hz frequency at 0.175 mW mm^{-2} (Fig. S7†). The mean PV value of the last 10 responses is the same as the first 10 responses, indicating that PVMs did not show any sign of fatigue over repetitive stimulation.

2.3 Colloidal self-assembly of PVMs

After showing that PVMs exhibit photoelectric properties that are promising for clinical applications, we aimed to validate the concept of *in situ* colloidal assemblies of PVMs into a coherent array within a confining curved cavity. We fabricated a biomimetic phantom from PDMS by modifying the concave surface of the cavity with gelatin. The gelatin layer recapitulates the compliance and chemical properties of the retinal surface.[45,46] The self-assembly method has three steps as illustrated in Fig. 1a. We injected a suspension of PVMs in an organic solvent, Novec 7100, into the retinal phantom. PVMs spontaneously

Open Access Article. Published on 03 July 2023. Downloaded on 12/24/2025 11:41:32 PM.
This article is licensed under a Creative Commons Attribution-NonCommercial 3.0 Unported Licence.

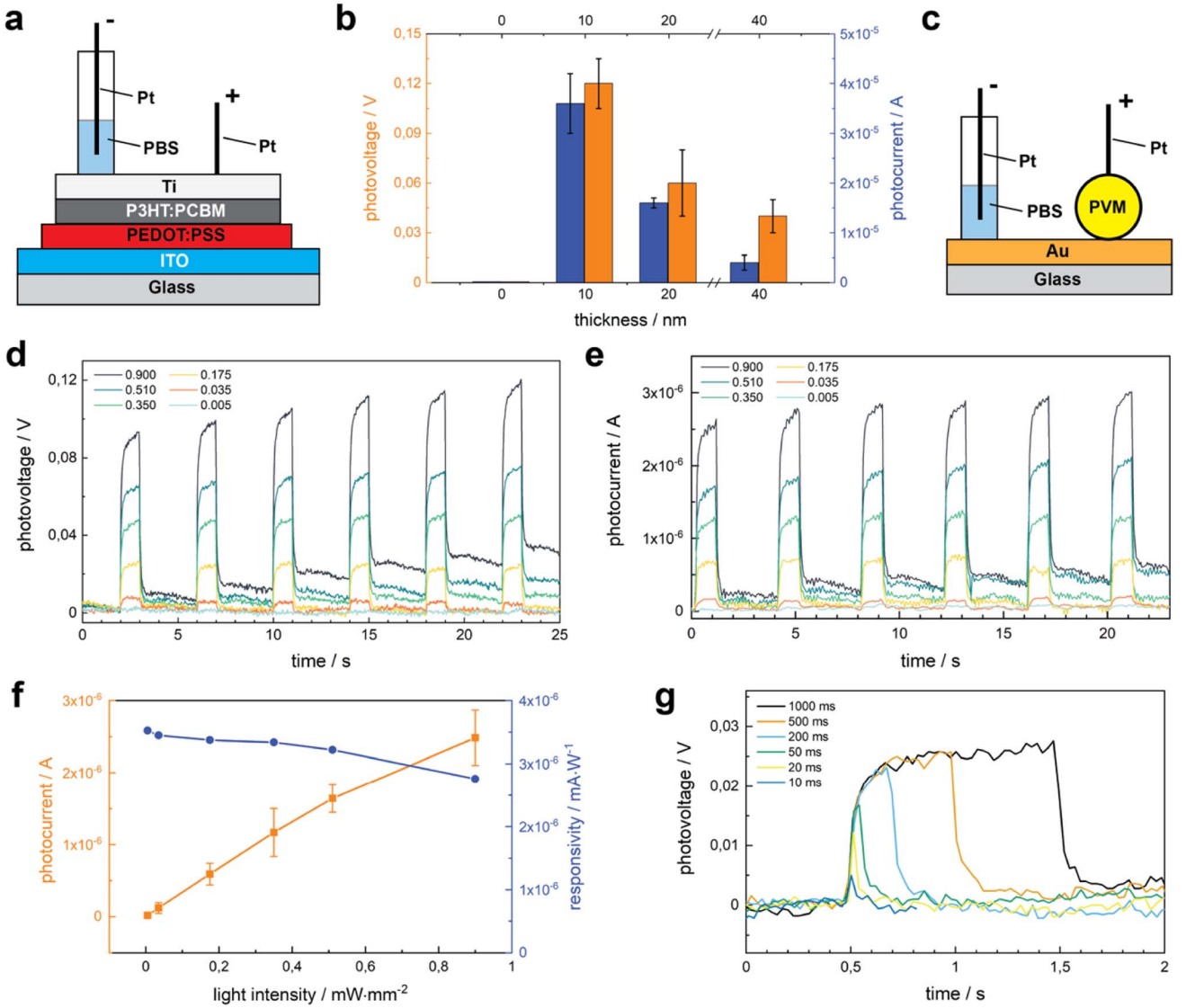

Fig. 3 Characterization of the PVMs. (a) Schematic illustration showing thin film devices in the form of glass@PEDOT:PSS@P3HT:PCBM@Ti. (b) PV and PC of thin film devices with different thicknesses of Ti upon 0.67 mW mm^{-2} illumination. Each bar represents measurements from 6 devices. (c) Schematic illustration of the experimental setup for PVM measurements. (d) PV and (e) PC of a PVM measured upon illumination with repeated 1 s pulses at increasing light power intensity. (f) Dependence of PC and responsivity on light power intensity. (g) Representative measurements from a PVM illuminated at a power intensity of 0.175 mW mm^{-2} and for different pulse duration.

formed a monolayer at the liquid–air interface. We then removed the solvent by evaporation or draining with an external aspiration pump. This process leaves a monolayer of PVMs on the curved substrate with a pattern that depends on the particle concentration, the composition of the suspension, and the rate at which the solvent is removed from the phantom.

First, we varied the concentration of PVMs. The concentration at which PVMs can fully cover the curved surface of the phantom is taken as 100%. Decreasing the PVM concentration from 100% to 25% results in rings of decreasing width that contain a close-packed assembly of PVM (Fig. 4a). Next, we utilized a biocompatible surfactant, Pico-Surf, to obtain further control over the PVM assembly. We suspended PVMs (25%) in the solvent at varying surfactant concentrations up to 1% (w/w). The suspensions were transferred to the phantom and exposed to air for the solvent to evaporate, leaving the self-assembled colloidal film behind. Due to the high volatility of the solvent, this process takes less than 3 min. In the absence of the surfactant, PVMs formed the so-called coffee-rings where particles accumulate near the contact line due to the outward evaporation-driven capillary flow. We did not observe a significant change in the final shape of the assembly, even when the concentration of surfactant was 1% (w/w) (Fig. 4b). The size of the surfactant molecule is significantly smaller than the diameter of PVMs, therefore it does not seem to play an important role in the agglomeration of the PVMs.

We postulated that the assembly pattern could be modified by tuning the rate at which the solvent is removed from the

© 2023 The Author(s). Published by the Royal Society of Chemistry

Open Access Article. Published on 03 July 2023. Downloaded on 12/24/2025 11:41:32 PM.
This article is licensed under a Creative Commons Attribution-NonCommercial 3.0 Unported Licence.

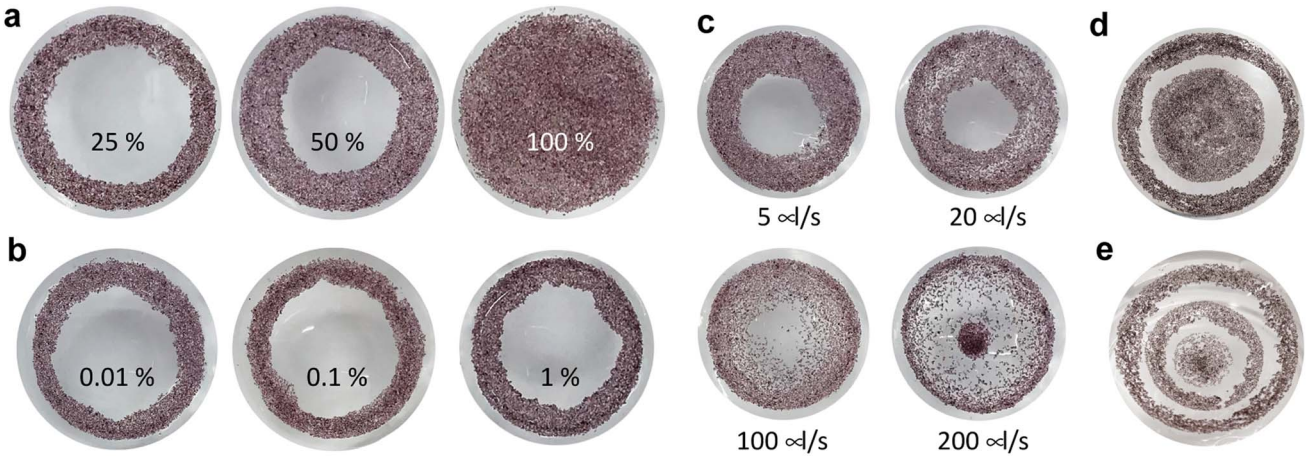

Fig. 4 Self-assembly of PVMs at the liquid–air interface. (a) PVM concentration and surface coverage inside the retina phantom. (b) The effect of surfactant concentration on PVM distribution and patterning. (c) Patterning PVMs using controlled liquid aspiration. Pattern formation through iterative injection of PVMs with two (d) and three (e) evaporation steps. The diameter of the hemispherical phantom is 14 mm.

phantom. To this end, we drained the phantom through aspiration using a syringe pump and polymer tubing. The tube was gently inserted from the center of the suspension. We explored the self-assembly of PVMs (60%) at various flow rates up to 200 μl s^{-1} (Fig. 4c). At 5 μl s^{-1}, the final pattern is very similar to the one obtained *via* evaporation at room temperature. With increasing flow rate, the particles covered a larger area with a distribution that got sparser from the edge to the center. When the flow rate reached 200 μl s^{-1}, a discontinuity appeared where a portion of PVMs was brought to the tubing and deposited in the center of the surface. More complex patterns could be instantiated by manipulating conditions in a combinatorial way. As an example, we prescribed concentric regions with an empty annulus in between by first depositing PVMs (25%), followed by the deposition of another batch of PVMs (50%), both through the evaporation of the solvent (Fig. 4d). The number of circles could be increased by increasing the number of deposition steps (Fig. 4e).

The retina is a thin layer of tissue that lines the back of the eye on the inside. The eyeball is filled with a viscoelastic fluid

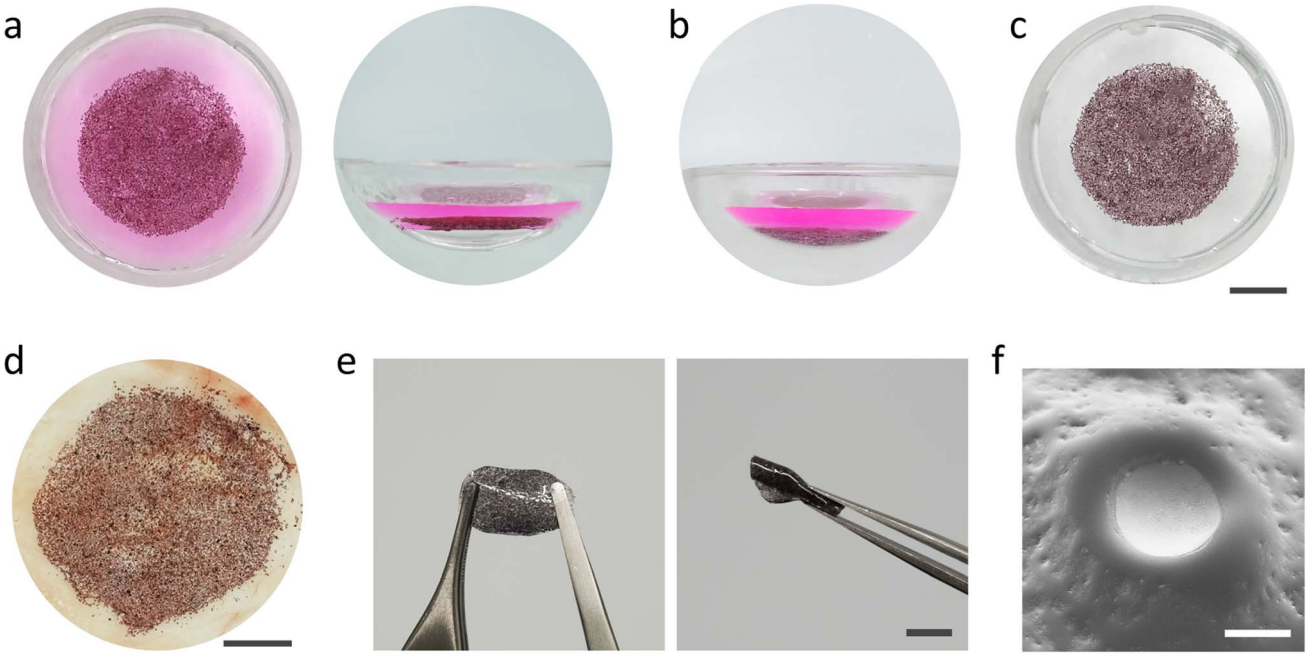

Fig. 5 Self-assembly of PVMs at the liquid–liquid interface and polymer integration. (a) A monolayer of PVMs forms at the water–oil interface. The physiological solution is dyed pink. (b) Self-assembled PVM film is transferred to the surface of the retinal phantom by aspirating the oil phase. (c) Self-assembled PVM film after the complete removal of the physiological fluid. (d) Self-assembly of PVMs on the chicken fascia. (e) PVM array embedded within a flexible polymer. Scale bars, 5 mm. (f) SEM image of a PV pixel on the polymer device. Scale bar, 40 μm.

Open Access Article. Published on 03 July 2023. Downloaded on 12/24/2025 11:41:32 PM.
This article is licensed under a Creative Commons Attribution-NonCommercial 3.0 Unported Licence.

called the vitreous humor. We asked whether PVMs could be assembled at a liquid–liquid interface that would be formed inside the eyeball and whether this assembly could be deposited on the retina with the removal of the injected fluid. We filled the chamber of the phantom with a phosphate buffered solution (PBS) mixed with rhodamine B dye to be able to distinguish the injected fluid. A suspension of PVMs (100%) in the organic solvent was injected into the PBS solution. The solution remained at the bottom of the chamber due to its density, and the PVMs instantaneously floated to the liquid–liquid interface where they will remain indefinitely due to surface energy minimization (Fig. 5a). Draining the solvent using a syringe pump moved the PVM monolayer to the substrate, conforming to the surface curvature (Fig. 5b). The dyed PBS solution was removed to clearly observe the assembled device (Fig. 5c).

As a further demonstration of biomedical relevance, we utilized chicken fascia, which primarily consists of collagen, to better mimic the texture and chemistry of the retina surface. We followed the same injection, self-assembly, and transfer operation as we did with the elastomer phantom. Once again, the PVMs self-assembled into a monolayer which conformed and adhered to the surface of the fascia at the end of the draining process (Fig. 5d). The PVM monolayer remained attached to the tissue as we gently washed the surface with water. The strong adhesion might be due to the reported adhesive properties of Ti surfaces to proteins.[47,48] The presented process is a facile strategy for self-assembling colloidal electronics into large-area prosthetics underwater.

As illustrated in Fig. 1, once PVMs are distributed onto the target surface, a polymer precursor can be injected and photopolymerized *in situ* to protect the integrity of the device. Ideally, the polymer precursor must be biocompatible, transparent, photocurable, and injectable, and the polymer must be flexible to avoid delamination issues. As a preliminary attempt, we used a polymer precursor composed of poly(ethylene glycol) phenyl ether acrylate (EGPEA) as a monomer, poly(ethylene glycol) diacrylate (PEGDA) as a crosslinker, and Irgacure-819 as visible light initiator. We injected the precursor and performed the photopolymerization process inside the phantom. The PVM–polymer composite substrate is stretchable and flexible (Fig. 5e). Fig. 5f shows a close-up view around a single PVM where part of the cathode is exposed, which serves as an electronic interface with the underlying tissue.

3. Conclusion

We presented a design and fabrication methodology for photovoltaic microdevices (PVMs) as injectable colloids. Using photovoltaic microparticles, we aim to combine the superior performance and controllable architecture of centimeter-scale microfabricated devices[2–7] with the accessibility and minimally invasiveness of photovoltaic nanoparticles.[15–17] We showed that the voltage transduced by PVMs could reach the levels that would effectively activate retinal neural layers.[6,42–44] The methodology is tunable in terms of layer thicknesses, and compatible with smaller pixels (down to a few micrometers). Based on the literature,[6,31] we postulate that Ti layer serves as a capacitive charge injection material. However, further research is required to gain a detailed understanding of the potential faradaic or capacitive processes that occur at the interface, which is instrumental to develop and optimize future devices. This problem has been recently studied with organic photoelectrodes based on a planar p–n junction containing phthalocyanine (H_2Pc) and *N*,*N*′-dimethyl perylenetetracarboxylic diimide (PTCDI).[49] The results show that in the floating configuration, which is analogous to our settings, the photoelectrode automatically charges positively and operates in the purely capacitive mode, supporting our initial hypothesis.

As a first step towards developing an *in situ* assembly process that is compatible with the anatomy and physiology of the eye, we studied self-assembly at the liquid–air and liquid–liquid interfaces. PVMs that are suspended in physiological fluids such as PBS float to the interface where the relative interfacial tension drives them to form specific monolayer patterns. We systematically varied key parameters including PVM concentration, liquid drain speed, and self-assembly times to control the final configuration of the assembly. We can envision personalized treatments where only the defective part of the retina is interfaced with PVMs while vision in the remaining regions is performed by the native biological sensors. To this end, we have to engineer additional control mechanisms to instantiate pattern formation at the liquid–liquid interface inside the eye, and seamlessly transfer this assembly onto the retina through aspiration.

Once assembled on the retina, the PVMs are expected to remain in place. To this end, we explored the potential of using an adhesive that is transparent, injectable, and photocurable. These results show that the overall methodology is promising for the facile *in situ* assembly and interfacing of both epi-retinal and sub-retinal prostheses. In order for this technology to be considered for clinical applications, the organic photovoltaic interface must be optimized for higher stability, better optoelectronic performance, and adjusted sensitivity. The PEDOT:PSS layer has poor stability inside physiological media due to the hydrophilicity of the PSS. As the material swells, the thin film delaminates from the hydrogel core. One possible solution is to tune the crosslinking density of the PEDOT:PSS layer. The chemistry of the interfaces between this layer and the surrounding layers could also be optimized for attachment. The size, mechanical and structural properties of the PVMs must be studied considering the operation of injection into the eye ball and the subsequent assembly steps.

4. Experimental methods

All reagents were purchased from Sigma-Aldrich and used as received unless otherwise stated.

4.1 Fabrication of photovoltaic particles

The PTPETA@PEDOT:PSS particles were synthesized *via* droplet microfluidics using a microchannel that is 100 μm wide and 100 μm tall. Microchannels were fabricated using replica molding. Solutions and suspensions were injected into the microfluidic

© 2023 The Author(s). Published by the Royal Society of Chemistry

Open Access Article. Published on 03 July 2023. Downloaded on 12/24/2025 11:41:32 PM. This article is licensed under a Creative Commons Attribution-NonCommercial 3.0 Unported Licence.

device using a computer controlled syringe pump (neMESYS 290N, Cetoni). The inner, middle, and continuous phases consist of TPETA with 0.1% (w/w) Daracure 1173, PEDOT:PSS aqueous solution with 0.1% (w/w) Tween 20, and Novec 7100 with 0.1% (w/w) Pico-Surf, respectively. Double emulsion of TPETA@PEDOT:PSS was formed and the collection tube was irradiated at 365 nm (5 mW cm^{-2}) for 10 s to polymerize the TPETA. The suspension was incubated in Novec 7500 with 1% (w/w) Pico-Surf at 93 °C for 1 h. The PTPETA@PEDOT:PSS particles were washed 3 times with Novec 7100 to remove Novec 7500. The final PTPETA@PEDOT:PSS particles were suspended in Novec 7100 for storage and further experimentation. 3 mg P3HT and 3 mg PCBM were dissolved in 1 ml chloroform (CF) and heated at 60 °C for 24 h. Meanwhile, PTPETA@PEDOT:PSS suspension in Novec 7100 was deposited on a net filter with 40 μm mesh size and heated at 120 °C for 30 min. The filter with particles was immersed into P3HT:PCBM solution and extracted. Thanks to the volatile nature of CF, P3HT:PCBM forms a thin film covering the PTPETA@PEDOT:PSS particles. This process was repeated 3 times to ensure conformal coating. PTPETA@PEDOT:PSS@P3HT:PCBM particles were heated at 120 °C for 30 min to finish the coating. Ti was sputtered on PTPETA@PEDOT:PSS@P3HT:PCBM particles in 3 consecutive sessions in the cleanroom (EVA 760). PTPETA@PEDOT:PSS@P3HT:PCBM@Ti particles were stored under vacuum and complete darkness.

4.2 Fabrication of 2D photovoltaic sheets

Photovoltaic films were fabricated on a glass slide (15 mm × 10 mm) that was cleaned by sonication in deionized water, acetone and isopropanol for 15 min successively, and dried with compressed air. A 100 μm thick ITO layer was deposited on the glass slide through sputtering (EVA 760). PEDOT:PSS (AL 4083, Ossila) was spin-coated at 3000 rpm for 60 s on the chip, then annealed at 120 °C for 30 min. In the following step, P3HT:PCBM solution (3 mg P3HT, 3 mg PCBM, 1 ml chlorobenzene) was spin-coated at 1000 rpm for 60 s, and annealed at 120 °C for 30 min. Ti cathodes were deposited through sputtering (EVA 760). The films were stored under a vacuum and in complete darkness.

4.3 Electrical measurements

PVMs were placed on a conductive glass slide coated with a 100 nm thick gold layer. A capillary reservoir was attached to the glass slide and a platinum wire was immersed in the physiological saline solution, phosphate-buffered saline (PBS), as the reference electrode. The measurements were performed on single PVMs. The measurement probe, a platinum wire, was connected to a single PVM using a robotic micromanipulator (SmarAct GmbH) mounted on a stereo microscope (Leica M165 C). The micromanipulator has 3 degrees of freedom (XYZ, SLC1740me-14,-15,-16) with 4 nm resolution. The particles were illuminated at 565 nm using a computer-controlled light source (SOLA SE II) with a 550 nm bandpass filter located at the tip of the light guide. The duration, frequency, and intensity of light were modulated *via* the electronic shutter that is controlled by the open-source μManager software. PV and PC measurements were done using a source meter (B2902A, Keysight).

4.4 Fabrication of the biomimetic phantom

The eye phantom was fabricated using a silicon-based organic polymer. Degassed polydimethylsiloxane (PDMS) precursor (10 : 1, SYLGARD, Dow Corning, USA) was cast in a cylinder container. A glass sphere that is 25 mm in diameter was half pressed into the PDMS precursor. Next, the PDMS precursor was cured in an oven at 65 °C for 12 h. The curved surface of the phantom was coated with gelatin by immersing the substrate first in 0.01% (w/v) dopamine solution in 1 M Tris–HCl buffer (pH = 8.5) at 4 °C for 1 h, and then in 0.1% (w/v) gelatin solution in deionized (DI) water at 37 °C for 12 h. The surfaces were thoroughly washed with DI water 3 times.

4.5 Self-assembly process

PVMs were suspended in an organic solvent, Novec 7100 (3M). The suspension was gently mixed before transferring 500 μl of this suspension to the phantom. The drainage of the solvent was done using a 1 ml syringe that was mounted on a syringe pump (Harvard Apparatus). Assemblies were visualized using a digital camera (Sony DSC-RX100 VI) that is mounted on a stereo microscope (Nikon SMZ1270).

4.6 Statistical analysis

Results are presented as mean ± standard deviation. Statistical analysis was performed using Origin 2021 (OriginLab). Each measurement was repeated at least 3 times for each device and at least 6 different devices were tested for each condition.

Author contributions

H. J. and M. S. S. conceived the idea, acquired funding, and designed the experiments. H. J., Z. H., and M. K. performed the experiments. H. J. analyzed the data. H. J. and M. S. S. wrote the manuscript. M. S. S. supervised the project.

Conflicts of interest

There are no conflicts of interest to declare.

Acknowledgements

This work was supported by the SNSF Spark grant (Grant No. 8001). We thank Ecole Polytechnique Fédérale de Lausanne (EPFL) Center of MicroNano Technology (CMi) staff for their technical assistance and members of the MicroBioRobotic Systems (MICROBS) Laboratory for their intellectual feedback.

References

1 S. R. Flaxman, R. R. A. Bourne, S. Resnikoff, P. Ackland, T. Braithwaite, M. V. Cicinelli, A. Das, J. B. Jonas, J. Keeffe, J. Kempen, J. Leasher, H. Limburg, K. Naidoo, K. Pesudovs, A. Silvester, G. A. Stevens, N. Tahhan, T. Wong, H. Taylor,

Open Access Article. Published on 03 July 2023. Downloaded on 12/24/2025 11:41:32 PM.
This article is licensed under a Creative Commons Attribution-NonCommercial 3.0 Unported Licence.

A. Arditi, Y. Barkana, B. Bozkurt, A. Bron, D. Budenz, F. Cai, R. Casson, U. Chakravarthy, J. Choi, N. Congdon, R. Dana, R. Dandona, L. Dandona, I. Dekaris, M. Del Monte, J. Deva, L. Dreer, L. Ellwein, M. Frazier, K. Frick, D. Friedman, J. Furtado, H. Gao, G. Gazzard, R. George, S. Gichuhi, V. Gonzalez, B. Hammond, M. E. Hartnett, M. He, J. Hejtmancik, F. Hirai, J. Huang, A. Ingram, J. Javitt, C. Joslin, M. Khairallah, R. Khanna, J. Kim, G. Lambrou, V. C. Lansingh, P. Lanzetta, J. Lim, K. Mansouri, A. Mathew, A. Morse, B. Munoz, D. Musch, V. Nangia, M. Palaiou, M. B. Parodi, F. Y. Pena, T. Peto, H. Quigley, M. Raju, P. Ramulu, D. Reza, A. Robin, L. Rossetti, J. Saaddine, M. Sandar, J. Serle, T. Shen, R. Shetty, P. Sieving, J. C. Silva, R. S. Sitorus, D. Stambolian, J. Tejedor, J. Tielsch, M. Tsilimbaris, J. van Meurs, R. Varma, G. Virgili, Y. X. Wang, N. L. Wang, S. West, P. Wiedemann, R. Wormald and Y. Zheng, *Lancet Global Health*, 2017, **5**, e1221.

2 E. Zrenner, K. U. Bartz-Schmidt, H. Benav, D. Besch, A. Bruckmann, V. P. Gabel, F. Gekeler, U. Greppmaier, A. Harscher, S. Kibbel, J. Koch, A. Kusnyerik, T. Peters, K. Stingl, H. Sachs, A. Stett, P. Szurma, B. Wilhelm and R. Wilke, *Proc. R. Soc. B*, 2011, **278**, 1489.

3 K. Mathieson, J. Loudin, G. Goetz, P. Huie, L. Wang, T. I. Kamins, L. Galambos, R. Smith, J. S. Harris, A. Sher and D. Palanker, *Nat. Photonics*, 2012, **6**, 391.

4 H. Lorach, G. Goetz, R. Smith, X. Lei, Y. Mandel, T. Kamins, K. Mathieson, P. Huie, J. Harris, A. Sher and D. Palanker, *Nat. Med.*, 2015, **21**, 476.

5 J. F. Maya-Vetencourt, D. Ghezzi, M. R. Antognazza, E. Colombo, M. Mete, P. Feyen, A. Desii, A. Buschiazzo, M. Di Paolo, S. Di Marco, F. Ticconi, L. Emionite, D. Shmal, C. Marini, I. Donelli, G. Freddi, R. MacCarone, S. Bisti, G. Sambuceti, G. Pertile, G. Lanzani and F. Benfenati, *Nat. Mater.*, 2017, **16**, 681.

6 L. Ferlauto, M. J. I. Airaghi Leccardi, N. A. L. Chenais, S. C. A. Gilliéron, P. Vagni, M. Bevilacqua, T. J. Wolfensberger, K. Sivula and D. Ghezzi, *Nat. Commun.*, 2018, **9**, 1.

7 P.-H. Prévot, K. Gehere, F. Arcizet, H. Akolkar, M. A. Khoei, K. Blaize, O. Oubari, P. Daye, M. Lanoë, M. Valet, S. Dalouz, P. Langlois, E. Esposito, V. Forster, E. Dubus, N. Wattiez, E. Brazhnikova, C. Nouvel-Jaillard, Y. LeMer, J. Demilly, C.-M. Fovet, P. Hantraye, M. Weissenburger, H. Lorach, E. Bouillet, M. Deterre, R. Hornig, G. Buc, J.-A. Sahel, G. Chenegros, P. Pouget, R. Benosman and S. Picaud, *Nat. Biomed. Eng.*, 2020, **4**, 172.

8 D. T. Hartong, E. L. Berson and T. P. Dryja, *Lancet*, 2006, **368**, 1795.

9 W. L. Wong, X. Su, X. Li, C. M. G. Cheung, R. Klein, C. Y. Cheng and T. Y. Wong, *Lancet Global Health*, 2014, **2**, e106.

10 K. Stingl, K. U. Bartz-Schmidt, D. Besch, C. K. Chee, C. L. Cottriall, F. Gekeler, M. Groppe, T. L. Jackson, R. E. MacLaren, A. Koitschev, A. Kusnyerik, J. Neffendorf, J. Nemeth, M. A. N. Naeem, T. Peters, J. D. Ramsden, H. Sachs, A. Simpson, M. S. Singh, B. Wilhelm, D. Wong and E. Zrenner, *Vis. Res.*, 2015, **111**, 149.

11 Y. H.-L. Luo and L. da Cruz, *Prog. Retinal Eye Res.*, 2016, **50**, 89.

12 M. J. I. Airaghi Leccardi, N. A. L. Chenais, L. Ferlauto, M. Kawecki, E. G. Zollinger and D. Ghezzi, *Commun. Mater.*, 2020, **1**, 1.

13 V. Paola, M. J. I. Airaghi Leccardi, C.-H. Vila, E. G. Zollinger, G. Sherafatipour, T. J. Wolfensberger and D. Ghezzi, *Nat. Commun.*, 2022, **13**, 1.

14 L. Gu, S. Poddar, Y. Lin, Z. Long, D. Zhang, Q. Zhang, L. Shu, X. Qiu, M. Kam, A. Javey and Z. Fan, *Nature*, 2020, **581**, 278.

15 J. F. Maya-Vetencourt, G. Manfredi, M. Mete, E. Colombo, M. Bramini, S. Di Marco, D. Shmal, G. Mantero, M. Dipalo, A. Rocchi, M. L. DiFrancesco, E. D. Papaleo, A. Russo, J. Barsotti, C. Eleftheriou, F. Di Maria, V. Cossu, F. Piazza, L. Emionite, F. Ticconi, C. Marini, G. Sambuceti, G. Pertile, G. Lanzani and F. Benfenati, *Nat. Nanotechnol.*, 2020, **15**, 698.

16 S. Francia, D. Shmal, S. Di Marco, G. Chiaravalli, J. F. Maya-Vetencourt, G. Mantero, C. Michetti, S. Cupini, G. Manfredi, M. L. DiFrancesco, A. Rocchi, S. Perotto, M. Attanasio, R. Sacco, S. Bisti, M. Mete, G. Pertile, G. Lansani, E. Colombo and F. Benfenati, *Nat. Commun.*, 2022, **13**, 1.

17 F. Benfenati and G. Lanzani, *Nat. Rev. Mater.*, 2021, **6**, 1.

18 K. Ariga, Y. Yamauchi, T. Mori and J. P. Hill, *Adv. Mater.*, 2013, **25**, 6477.

19 T. Shibata, K. Fukuda, Y. Ebina, T. Kogure and T. Sasaki, *Adv. Mater.*, 2008, **20**, 231.

20 D. Liu, W. Cai, M. Marin, Y. Yin and Y. Li, *ChemNanoMat*, 2019, **5**, 1338.

21 L. Hu, M. Chen, X. Fang and L. Wu, *Chem. Soc. Rev.*, 2012, **41**, 1350.

22 H. Xia and D. Wang, *Adv. Mater.*, 2008, **20**, 4253.

23 Z. Chai, A. Korkmaz, C. Yilmaz and A. A. Busnaina, *Adv. Mater.*, 2020, **32**, 1.

24 S. N. Varanakkottu, M. Anyfantakis, M. Morel, S. Rudiuk and D. Baigl, *Nano Lett.*, 2016, **16**, 644.

25 J. J. Armao and J. M. Lehn, *Angew. Chem., Int. Ed.*, 2016, **55**, 13450.

26 C. R. Kagan, *Chem. Soc. Rev.*, 2019, **48**, 1626.

27 R. Parreira, E. Özelçi and M. S. Sakar, *Adv. Intell. Syst.*, 2020, **2**, 2000062.

28 D. Ghezzi, M. R. Antognazza, M. Dal Maschio, E. Lanzarini, F. Benfenati and G. Lanzani, *Nat. Commun.*, 2011, **2**, 164.

29 D. Ghezzi, M. R. Antognazza, R. MacCarone, S. Bellani, E. Lanzarini, N. Martino, M. Mete, G. Pertile, S. Bisti, G. Lanzani and F. Benfenati, *Nat. Photonics*, 2013, **7**, 400.

30 D. Ghezzi, *Front. Neurosci.*, 2015, **9**, 1.

31 G. Manfredi, E. Colombo, J. Barsotti, F. Benfenati and G. Lanzani, *Annu. Rev. Phys. Chem.*, 2019, **70**, 99.

32 D. Dendukuri, D. C. Pregibon, J. Collins, T. A. Hatton and P. S. Doyle, *Nat. Mater.*, 2006, **5**, 365.

33 S. Marre and K. F. Jensen, *Chem. Soc. Rev.*, 2010, **39**, 1183.

34 N. N. Deng, W. Wang, X. J. Ju, R. Xie, D. A. Weitz and L. Y. Chu, *Lab Chip*, 2013, **13**, 4047.

© 2023 The Author(s). Published by the Royal Society of Chemistry

Open Access Article. Published on 03 July 2023. Downloaded on 12/24/2025 11:41:32 PM.
This article is licensed under a Creative Commons Attribution-NonCommercial 3.0 Unported Licence.

35 A. Håkansson, S. Han, S. Wang, J. Lu, S. Braun, M. Fahlman, M. Berggren, X. Crispin and S. Fabiano, *J. Polym. Sci., Part B: Polym. Phys.*, 2017, **55**, 814.
36 M. ElMahmoudy, S. Inal, A. Charrier, I. Uguz, G. G. Malliaras and S. Sanaur, *Macromol. Mater. Eng.*, 2017, **302**, 1.
37 K. M. Reza, S. Mabrouk and Q. Qiao, *Proc. Nat. Res. Soc.*, 2018, **2**, 02004.
38 K. Sun, S. Zhang, P. Li, Y. Xia, X. Zhang, D. Du, F. H. Isikgor and J. Ouyang, *J. Mater. Sci.: Mater. Electron.*, 2015, **26**, 4438.
39 J. Yu, Y. Zheng and J. Huang, *Polymers*, 2014, **6**, 2473.
40 S. Van Bavel, E. Sourty, G. De With, K. Frolic and J. Loos, *Macromolecules*, 2009, **42**, 7396.
41 S. F. Cogan, *Annu. Rev. Biomed. Eng.*, 2008, **10**, 275.
42 L. Höfling, J. Oesterle, P. Berens and G. Zeck, *Sci. Rep.*, 2020, **10**, 1.
43 A. Corna, T. Herrmann and G. Zeck, *J. Neural Eng.*, 2018, **15**, 045003.
44 L. Bareket, N. Waiskopf, D. Rand, G. Lubin, M. David-Pur, J. Ben-Dov, S. Roy, C. Eleftheriou, E. Sernagor, O. Cheshnovsky, U. Banin and Y. Hanein, *Nano Lett.*, 2014, **14**, 6685.
45 O. V. Khutoryanskaya, M. Potgieter and V. V. Khutoryanskiy, *Soft Matter*, 2010, **6**, 551.
46 Z. Tang, Y. Wang, P. Podsiadlo and N. A. Kotov, *Adv. Mater.*, 2006, **18**, 3203.
47 M. N. Sela, L. Badihi, G. Rosen, D. Steinberg and D. Kohavi, *Clin. Oral Implants Res.*, 2007, **18**, 630.
48 Y. Yang, R. Cavin and J. L. Ong, *J. Biomed. Mater. Res., Part A*, 2003, **67**, 344.
49 T. Paltrinieri, L. Bondi, V. Đerek, B. Fraboni, E. D. Głowacki and T. Cramer T, *Adv. Funct. Mater.*, 2021, **31**, 2010116.

© 2023 The Author(s). Published by the Royal Society of Chemistry